nature catalysis

Article

https://doi.org/10.1038/s41929-022-00887-z

Delocalization state-induced selective bond breaking for efficient methanol electrosynthesis from CO_2

In the format provided by the authors and unedited

Table of Contents:

Supplementary Notes

Supplementary Note 1. Electron interaction in EXAFS.

From a spectra experimental perspective, X-ray absorption spectra (XAS) can be described as follows:

$$\mu \approx \frac{\rho Z^4}{AE^3}$$

where μ (or μ(E)) is the absorption coefficient, Z is the atomic number, A is the atomic mass, E is the energy of X-ray, and ρ refers to sample density. This indicates the atomic type-based absorption feature.

On the other hand, modern quantum physics has given $\mu(E)$ of a bare atom with Fermi's Golden Rule as below[1]:

$$\mu(E) = |\langle i|H|f_0\rangle|^2$$

where $\langle i|$ represents the initial state (i.e., an X-ray, a core electron, and no photoelectron), $|f_0\rangle$ refers to the final state (i.e., no X-ray, a core-hole, and a photoelectron) of a bare atom, and H is the perturbation term.

The fine structure ($\chi(E)$) in molecules can thus be written as[1]:

$$\chi(E) \equiv \frac{\mu(E) - \mu_0(E)}{\Delta\mu_0(E)} \propto |\langle i|H|\Delta f\rangle|^2 \propto \int dr\delta(r)e^{ikr}\varphi_{scatt}(r) = \varphi_{scatt}(k, r = 0)$$

where $\mu_0(E)$ is a smooth background function representing the absorption coefficient of an isolated atom, and $\Delta\mu_0$ is the measured jump in the absorption μ(E) at the threshold energy E_0, and $|\Delta f\rangle = |f\rangle - |f_0\rangle$ is the effect of the neighboring atoms. This suggests that the EXAFS $\chi(E)$ is proportional to the wave function of the scattered photoelectrons.

Moreover, it is common to convert the X-ray energy to k (i.e., the wave number of the photoelectron), which has dimensions of 1/distance and is defined as:

$$k = \sqrt{\frac{2m(E - E_0)}{\hbar^2}}$$

where E_0 is the edge energy (e.g., ~8979 eV for Cu-K edge), E is the X-ray energy, and m refers to the electron mass. Thus, the k-space data $\chi(k)$ is also proportional to the amplitude of the scattered photoelectron at the absorbing atom.

Since the EXAFS signal majorly comes from the single scattering of photoelectrons between the absorbing atom and a neighboring atom, the wave function of scattered photoelectron can be roughly simplified as the probability of finding a scattered photoelectron in a quantum field consisting of these two atoms. According to the definition of the wave function, i.e., the probability of interaction at a certain time and position[2], the interaction information can be obtained from the EXAFS data.

Supplementary Note 2. Delocalization and HSAB theory.

Delocalization is a concept employed to describe the electron state. In solid materials, the delocalized electron refers to the electron that is subject to a weak periodic potential, so that it can move from one potential minimum to another under the influence of a small electric field, thermal energy, or even the uncertainty principle[3]. Generally, electron density distribution can be employed to describe the delocalization effect.

Based on the modern HSAB theory by Parr and Pearson[4, 5], the electronegativity (χ), chemical hardness (η), and electron energy (E_e) are closely related, the relationship can be described as follows:

$$\chi = -\left(\frac{\partial E_e}{\partial N}\right)_v$$

$$\eta = \frac{1}{2}\left(\frac{\partial^2 E_e}{\partial N^2}\right)_v$$

where N corresponds to the number of electrons, which can be obtained by the following definition in DFT:

$$\rho(r) = N \int d^3 r_2 \cdots \int d^3 r_N \Psi^*(r_1, r_2, \cdots r_N) \Psi(r_1, r_2, \cdots r_N)$$

in which $\rho(r)$ is the electron density distribution function, and Ψ is the wavefunction. As a result, chemical hardness can further be defined as below based on a recent report[6]:

$$\eta = \frac{1}{2}\left(\frac{\partial^2 E_e}{\partial \rho(r)^2}\right)_\nu$$

Based on the formula above, chemical hardness, similar to the delocalization effect, is also closely related to the electron density distribution. Previous studies have proposed a new definition of the softness kernel based on the exchange-correlation density and shown the relationship with the change of electron fluctuation upon external perturbation[6, 7]. To make the conclusion concise, it can be simply described as softer sites in molecules corresponding to a delocalization state. Moreover, in the multi-electron system, the delocalization effect refers to electron-density delocalization[8], i.e., a drop of electron density near the atomic nucleus as well as increased electron density away from the nucleus.

Supplementary Note 3. Additional details in computations and simulations.

Density functional theory (DFT) calculations were performed with the Vienna *ab initio* simulation package (VASP), using the plane-wave basis with an energy cutoff of 450 eV[9], projector augmented wave (PAW) potentials[10], and the generalized gradient approximation (GGA) with the Perdew-Burke-Ernzerhof (PBE) exchange-correlation functional[11]. In most situations, the Gaussian smearing method (with a width of 0.05) was used, while the tetrahedron method with Blöchl corrections[12] was applied for calculations on the density of states.

VASPKIT code (version 1.2.5)[13] was utilized for the establishment of the KPOINTS files

and data post-processing. The as-obtained data were processed by an electronic structure plotter module from Pymatgen package[14] with several modified codes to exhibit the intrinsic information of Cu_2NCN and Cu_2O.

For solvation corrections, this work employs an implicit solvation model within a linearized Poisson−Boltzmann approach based on VASPsol codes[15, 16]. According to previous studies on Cu_2O and metal surface[17, 18], a Debye screening length of 4.3 Å is chosen (i.e., corresponding to a bulk electrolyte concentration of 0.5 M) and the non-electrostatic coefficient is set to zero to avoid numerical instabilities in the electrolyte region[17].

For the transition state (TS) study, fully optimized slab models from Gibbs free energy calculations were employed as final states and initial states for a rough screening through the climbing image nudged elastic band (CI-NEB) method[19] with a fast inertial relaxation engine, and then the final structures of transition states were obtained by Dimer method with the convergence criterion of 10^{-7} eV, and the final residual force component was less than 0.02 $eV \cdot Å^{-1}$.

Moreover, the radial distribution function was obtained from the default algorithm in VMD software (version 1.9.3)[20, 21]. The calculated Infrared spectrum was obtained employing a density functional perturbation theory (DFPT) method[22-24] on a post-processing package JaGeo/IR[25].

Supplementary Figures

Supplementary Figure 1. **Photograph of as-synthesized Cu_2NCN.**

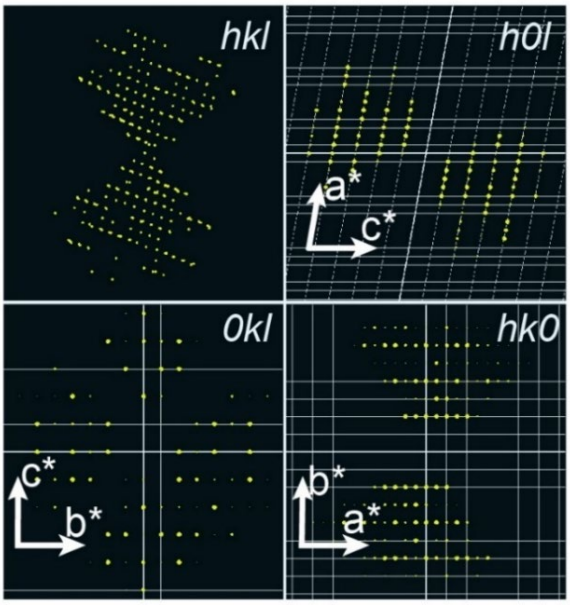

Supplementary Figure 2. Three-dimensional electron diffraction data. A monoclinic unit cell of a = 11.064(9) Å, b = 6.305(2) Å, c = 4.109(2) Å and β = 100.31(5)° was identified. All Cu, C and N atoms were located according to the combination of kinematical approximation structure solution and the common geometries of NCN^{2-} with the centrosymmetric space group P2/m.

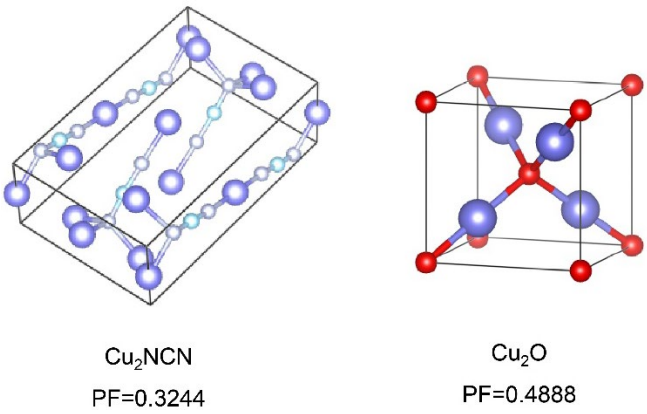

Supplementary Figure 3. Crystal packing factor (PF) of Cu_2NCN and Cu_2O. The PF value, which correlates to the structure openness, reveals the looser structure of Cu_2NCN[26]. The packing factor[27] was calculated as $PF = Z\,(xV_A + yV_B + zV_C)/V_{cell}$, where Z refers to the number of formula unit in one unit cell of a semiconductor ($A_xB_yC_z$); V_A, V_B, and V_C correspond to ion volumes calculated by assuming spherical ions with Shannon's radius; V_{cell} represents the cell volume.

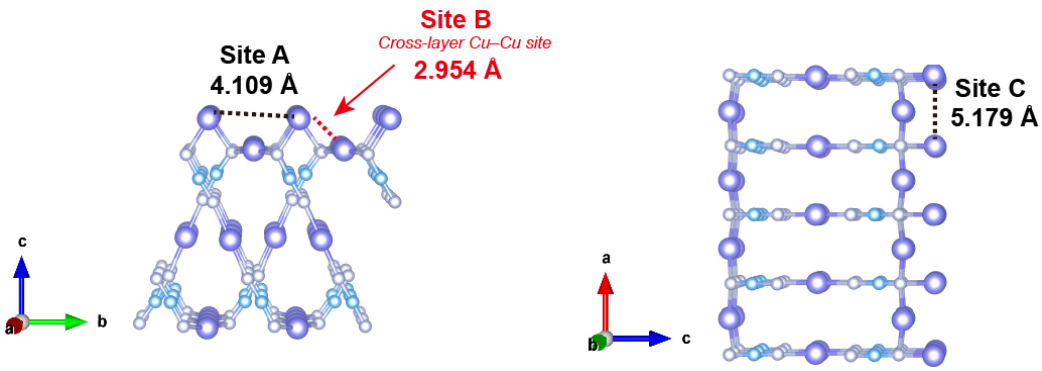

Supplementary Figure 4. Schematic illustration of coordinated Cu–Cu sites.

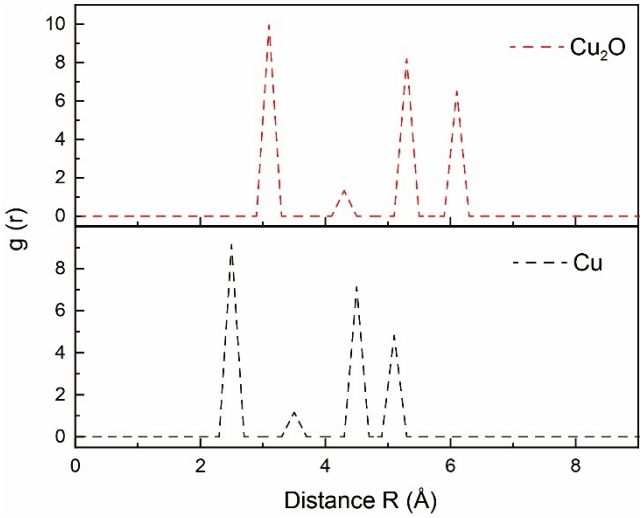

Supplementary Figure 5. The radial distribution function (g(r)) of Cu_2O (upper panel) and Cu (lower panel). Cu−Cu coordinates with a distance of < 3.5 Å contribute 41 ± 1% among all the coordinate types in Cu or Cu_2O.

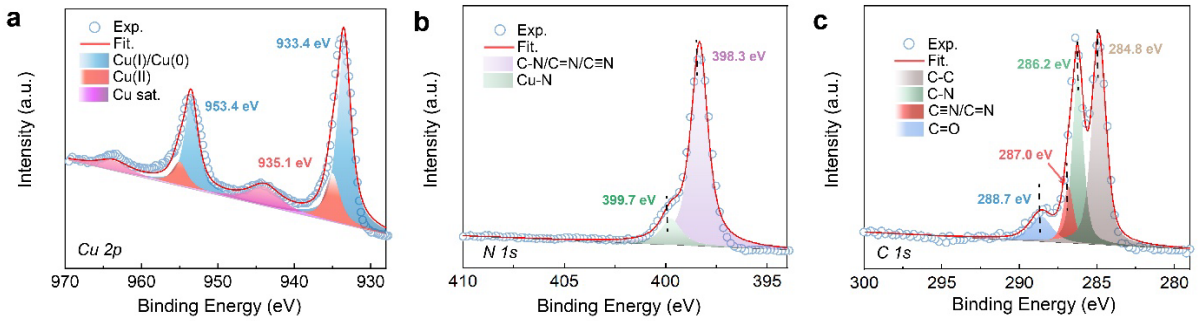

Supplementary Figure 6. High-resolution X-ray photoelectron spectroscopy (XPS) of Cu_2NCN. Deconvoluted spectra of (a) Cu 2p, (b) N 1s, and (c) C 1s.

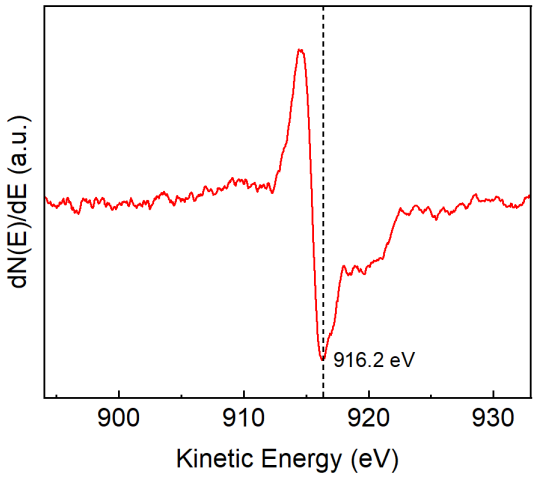

Supplementary Figure 7. Auger electron spectrum of Cu_2NCN (differential spectrum). The negative peak at 916.2 eV indicates the major Cu(I) phase on the Cu_2NCN surface.

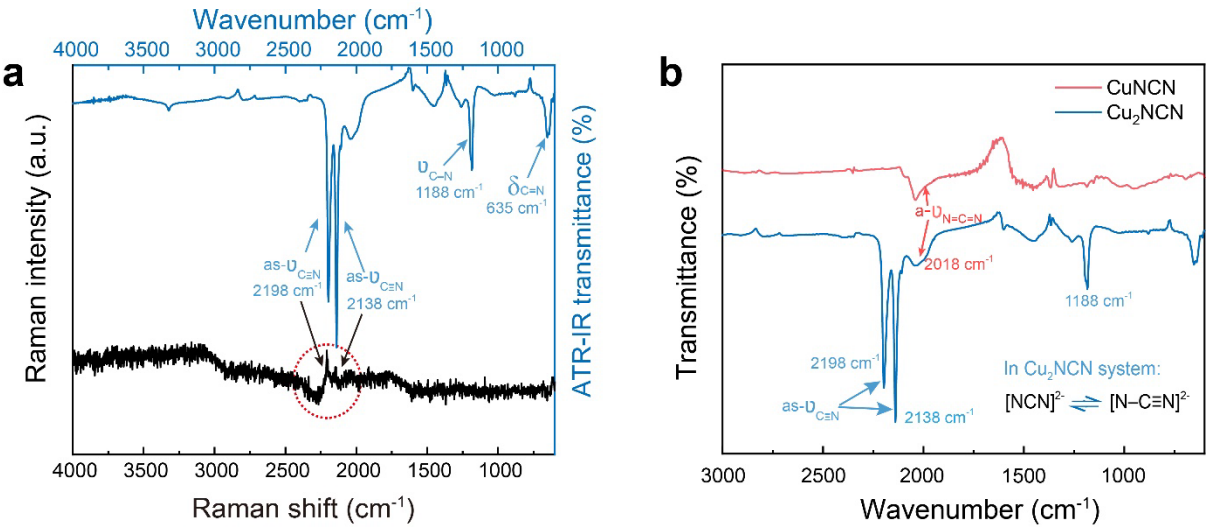

Supplementary Figure 8. Infrared and Raman spectra. (a) IR (blue curve, upper x-axis) and Raman (black curve, bottom x-axis) spectra of Cu_2NCN. (b) IR spectrum of Cu_2NCN (blue curve) and CuNCN (red curve). The vibration peaks confirm the major type of NCN^{2-} as $[N–C≡N]^{2-}$ in Cu_2NCN[28].

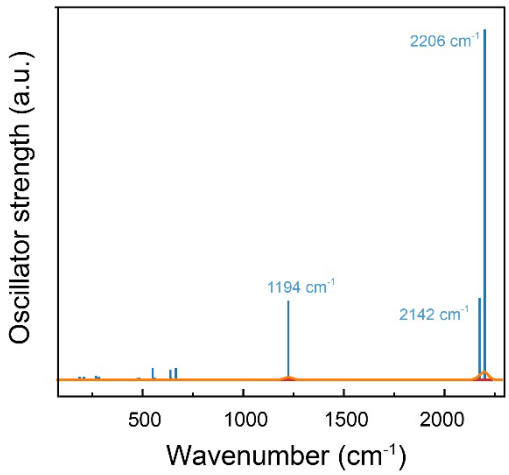

Supplementary Figure 9. Calculated IR spectrum of Cu_2NCN 3 × 3 × 1-super cell. The IR spectrum was calculated by the density functional perturbation theory method[22-25].

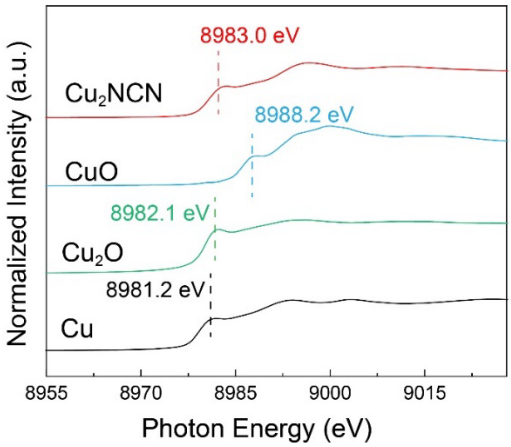

Supplementary Figure 10. XANES spectra of Cu_2NCN (red curve), in comparison with CuO, Cu_2O and Cu references.

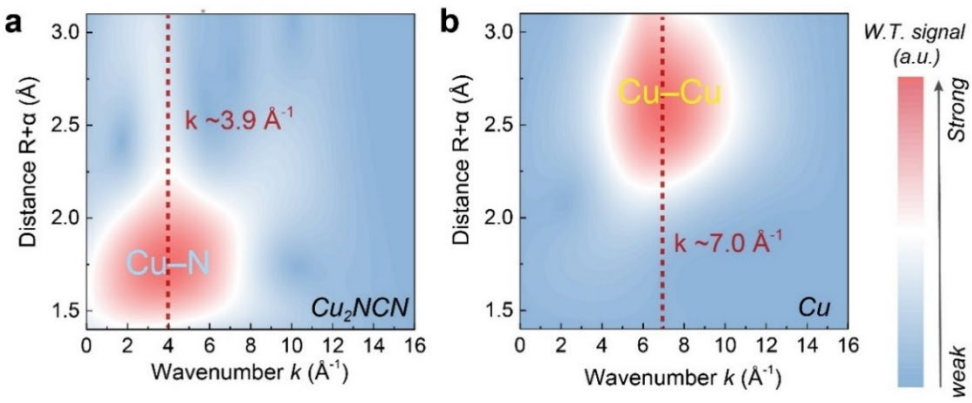

Supplementary Figure 11. Wavelet-transformed EXAFS spectra of (a) Cu_2NCN, (b) Cu, at the first coordination shell.

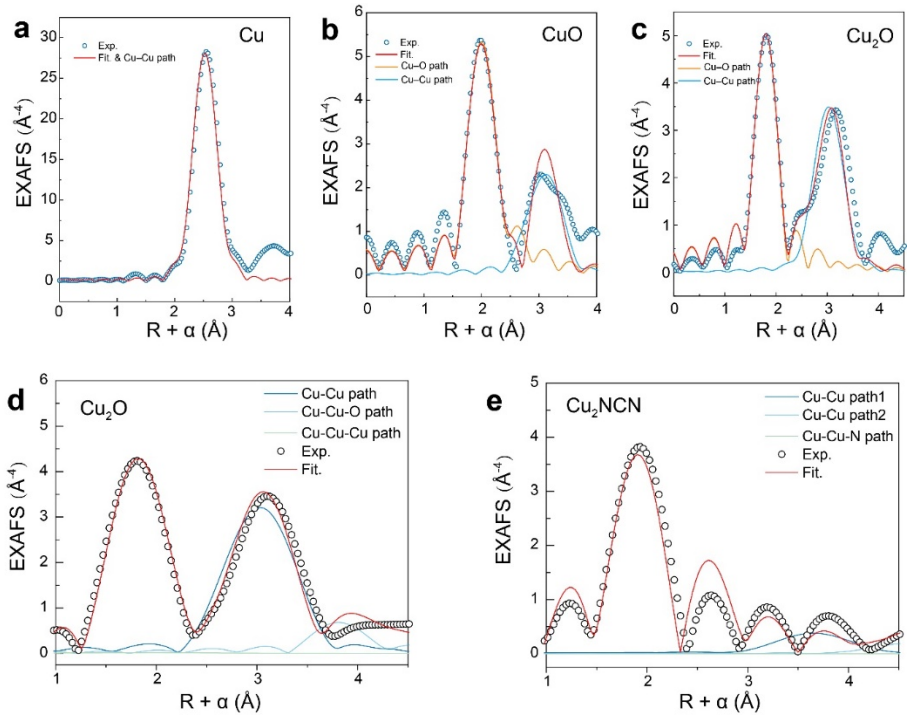

Supplementary Figure 12. Fourier-transformed EXAFS and corresponding fitting curves. Fitting at the first coordination shell (k range of data: 3.0−11 $Å^{-1}$) for (a) Cu foil, (b) CuO and (c) Cu_2O; multi-shell fitting (k range of data: 3.0−9.5 $Å^{-1}$) and the key Cu scattering paths for (d) Cu_2O and (e) Cu_2NCN.

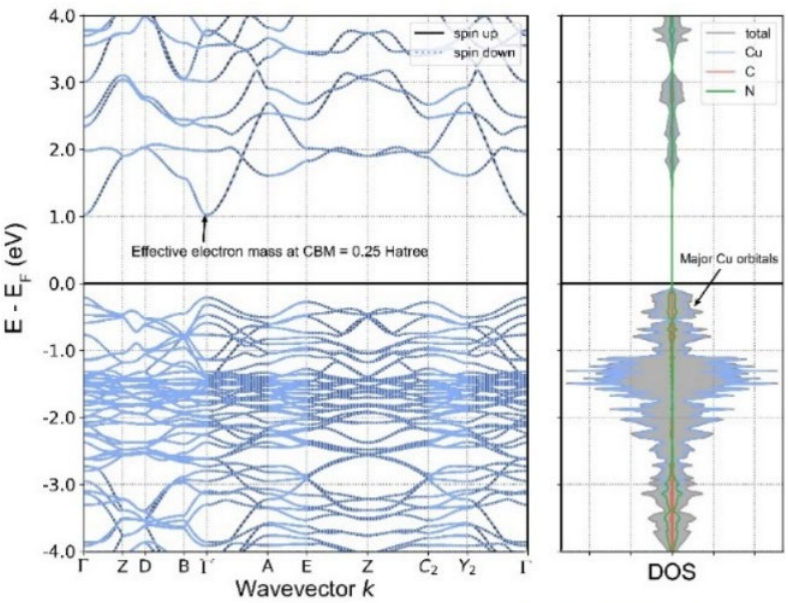

Supplementary Figure 13. Band structure (left) and density of states (DOS, right) of Cu_2NCN from DFT calculations. The effective electron mass at conduction band minimum (CBM) was calculated to be 0.25 Hartree. The DOS around Fermi level was mainly contributed by Cu orbitals.

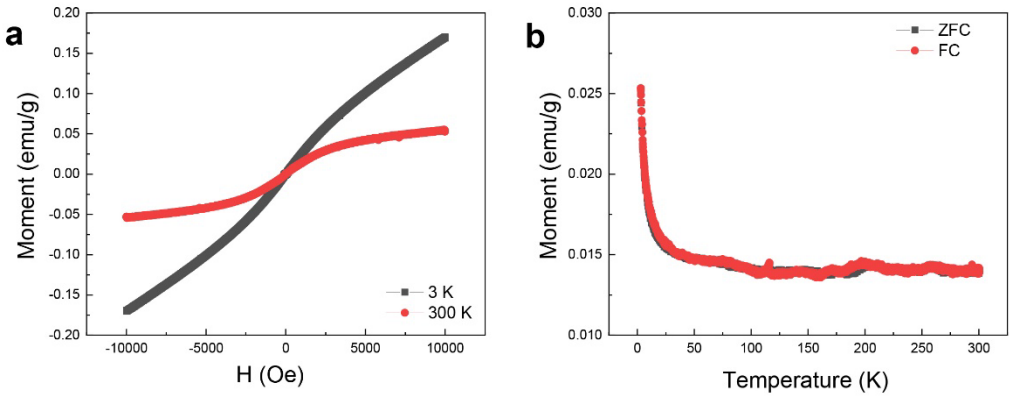

Supplementary Figure 14. Magnetic moment measurement. (a) Magnetic moment versus external magnetic field intensities. (b) Magnetic moment versus temperatures.

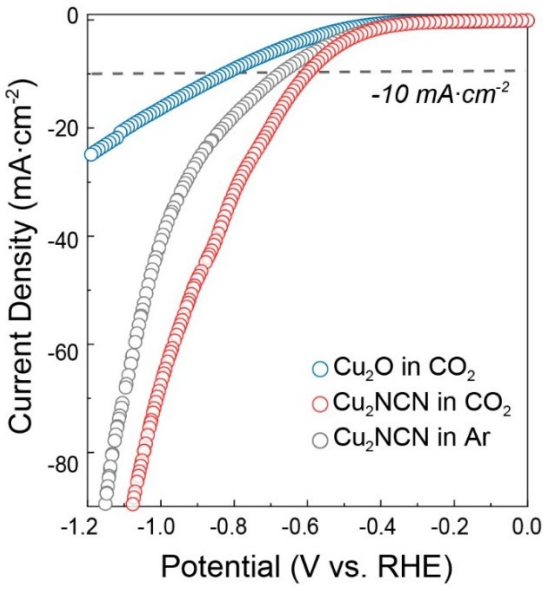

Supplementary Figure 15. Linear sweep voltammetry (LSV) curves. LSV of Cu_2O in CO_2-saturated electrolyte (red curve), Cu_2NCN in CO_2-saturated electrolyte (blue curve) and Ar-saturated electrolyte (black curve).

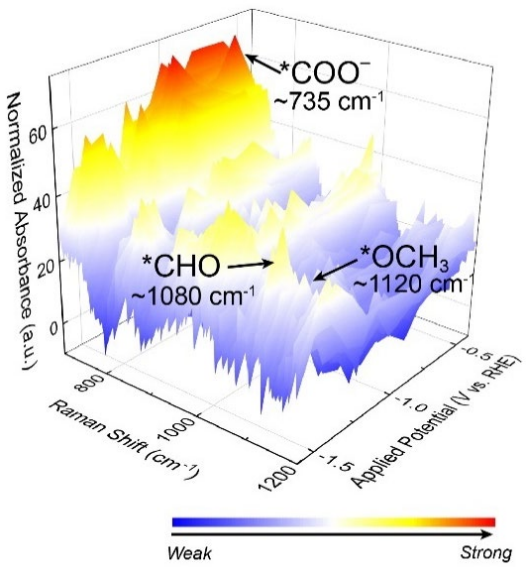

Supplementary Figure 16. In-situ electrochemical Raman spectra in CO_2RR of Cu_2NCN at an applied potential range from −0.5 to −1.5 V (vs. RHE).

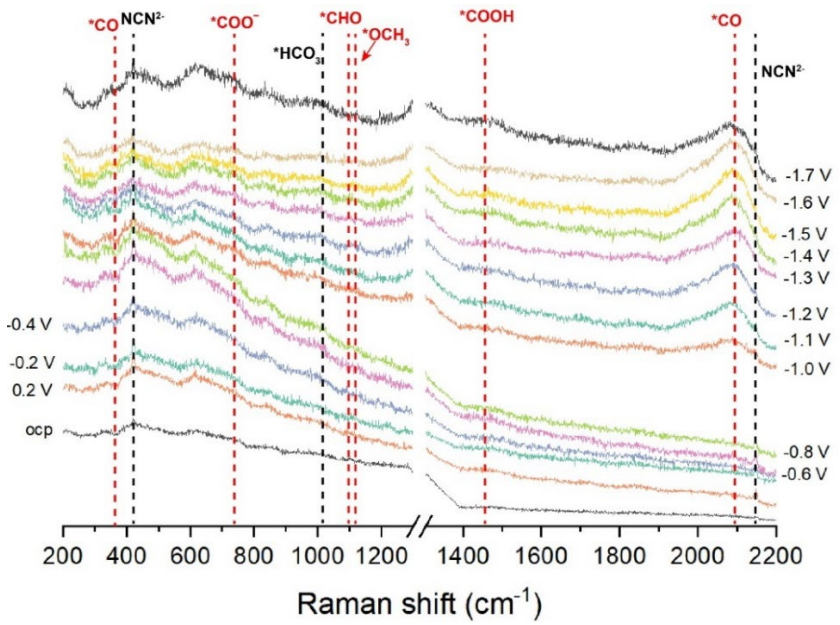

Supplementary Figure 17. **The 2D in-situ electrochemical Raman spectra of CO_2RR on Cu_2NCN.** The band of glassy carbon electrode (~ 1300 cm^{-1}) was removed.

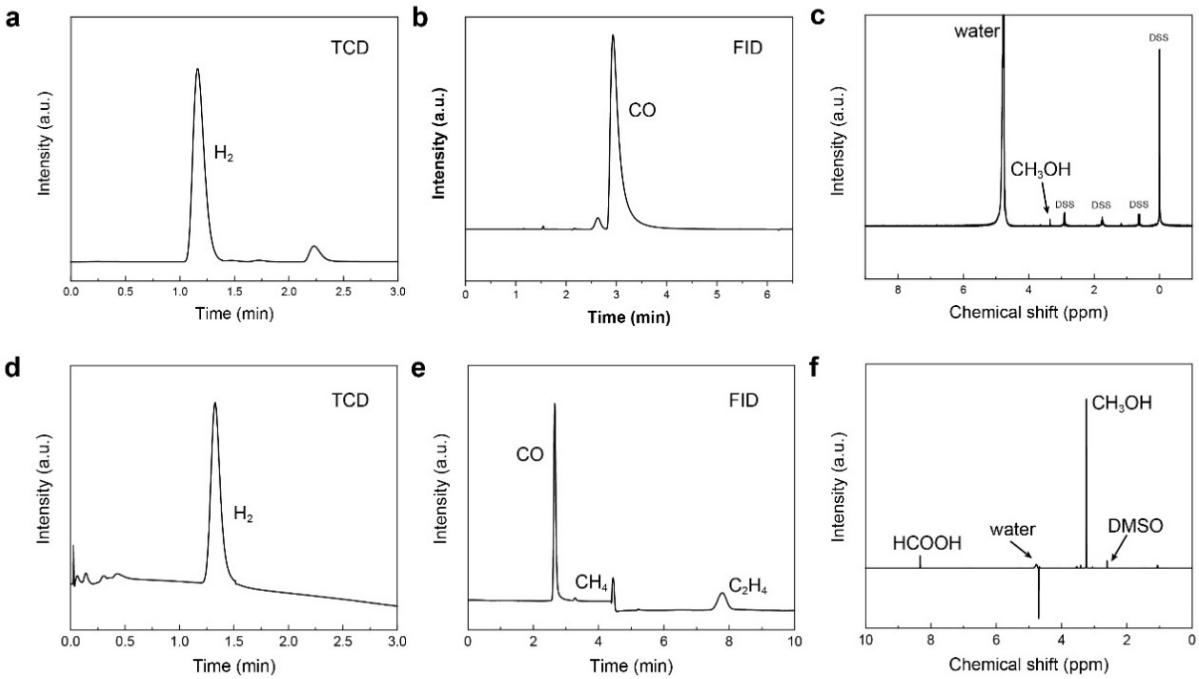

Supplementary Figure 18. Representative data on gas products and liquid products distributions. (a) TCD channel and (b) FID channel data for gas products from H-type cells at –0.67 V vs. RHE, and (c) liquid products analysis at the same conditions. (d) TCD channel and (e) FID channel data for gas products in MEA-based electrolyzer test at a full-cell voltage of 3.4 V, and (f) the liquid products analysis at the same conditions.

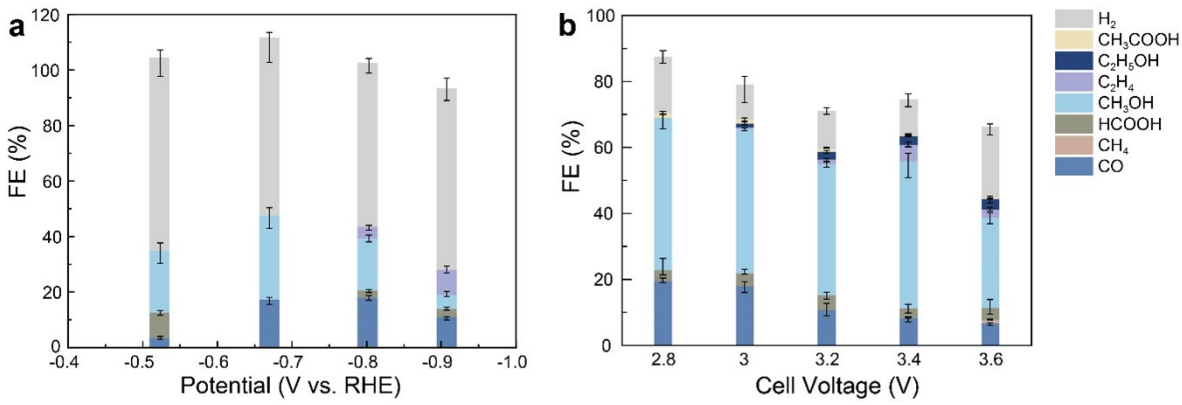

Supplementary Figure 19. Faradaic efficiency distributions of CO_2RR on Cu_2NCN. (a) Data collected in H-type cells; (b) Data collected in MEA-based electrolyzers. Data were presented in average (N = 3 refers to the number of repeated experiments; error bars represent standard deviations).

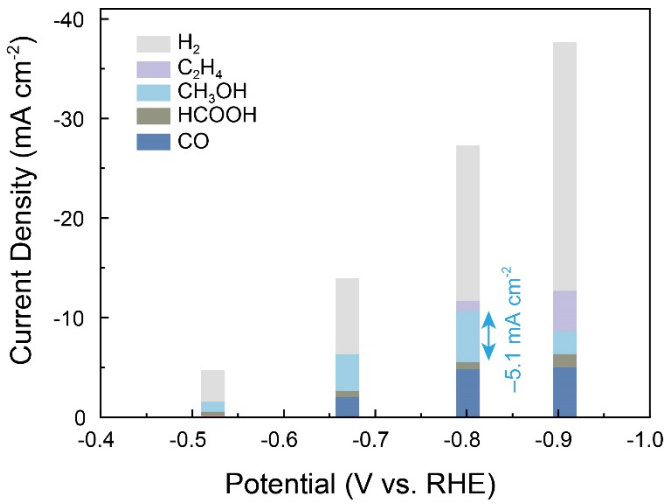

Supplementary Figure 20. **Partial current density of products on Cu_2NCN in H-type cells.** The CH_3OH partial current density of −5.1 mA·cm^{-2} was recorded at the potential of −0.80 V vs. RHE.

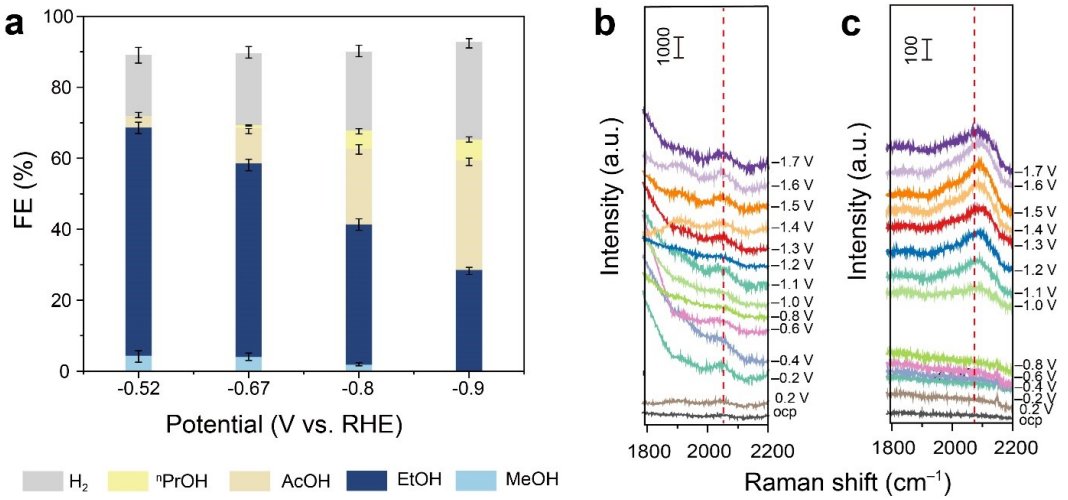

Supplementary Figure 21. Electrochemical CO reduction reaction (CORR) experiment. (a) FE distribution on Cu_2NCN for CORR, (b) the in-situ Raman spectra in a CO-saturated 0.1 M $KHCO_3$ solution, and (c) the in-situ Raman spectra in a CO_2-saturated 0.1 M $KHCO_3$ solution. FE data were presented in average (N = 3 refers to the number of repeated experiments; error bars represent standard deviations).

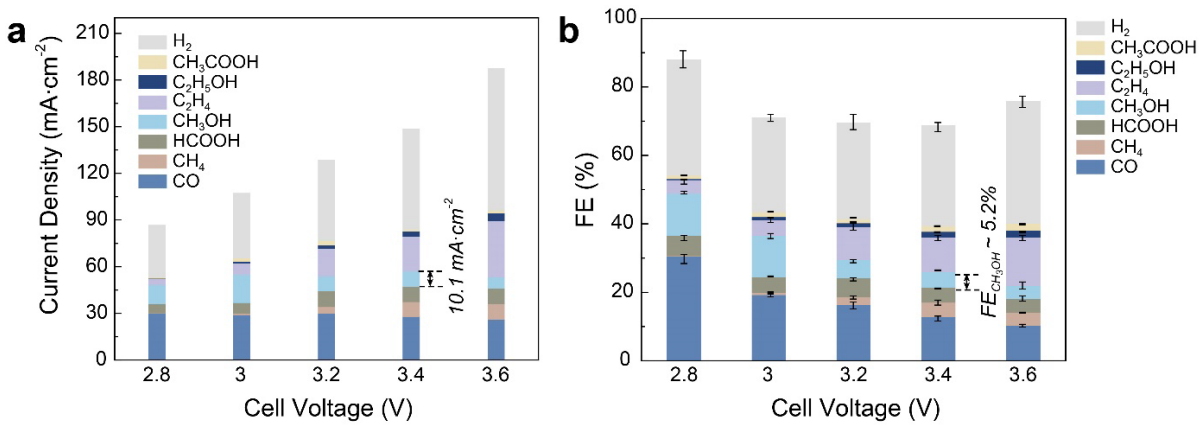

Supplementary Figure 22. CO_2RR performance of CuNCN in MEA. (a) Partial current density and (b) Faradaic efficiency distribution of different products on the CuNCN catalyst. Data were presented in average (N = 3 refers to the number of repeated experiments; error bars represent standard deviations).

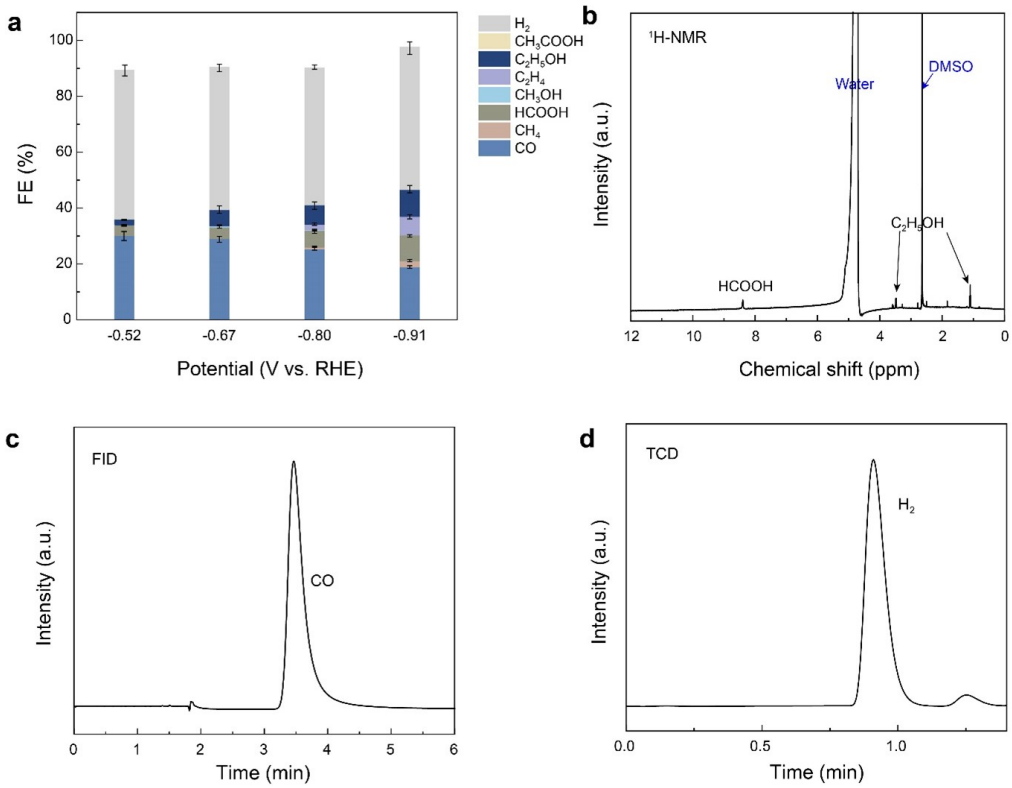

Supplementary Figure 23. **The CO_2RR performance of Cu_2O.** (a) FE distributions on Cu_2O and corresponding (b) ^{1}H-NMR, (c) GC-FID, (d) GC-TCD data. FE data were presented in average (N = 3 refers to the number of repeated experiments; error bars represent standard deviations).

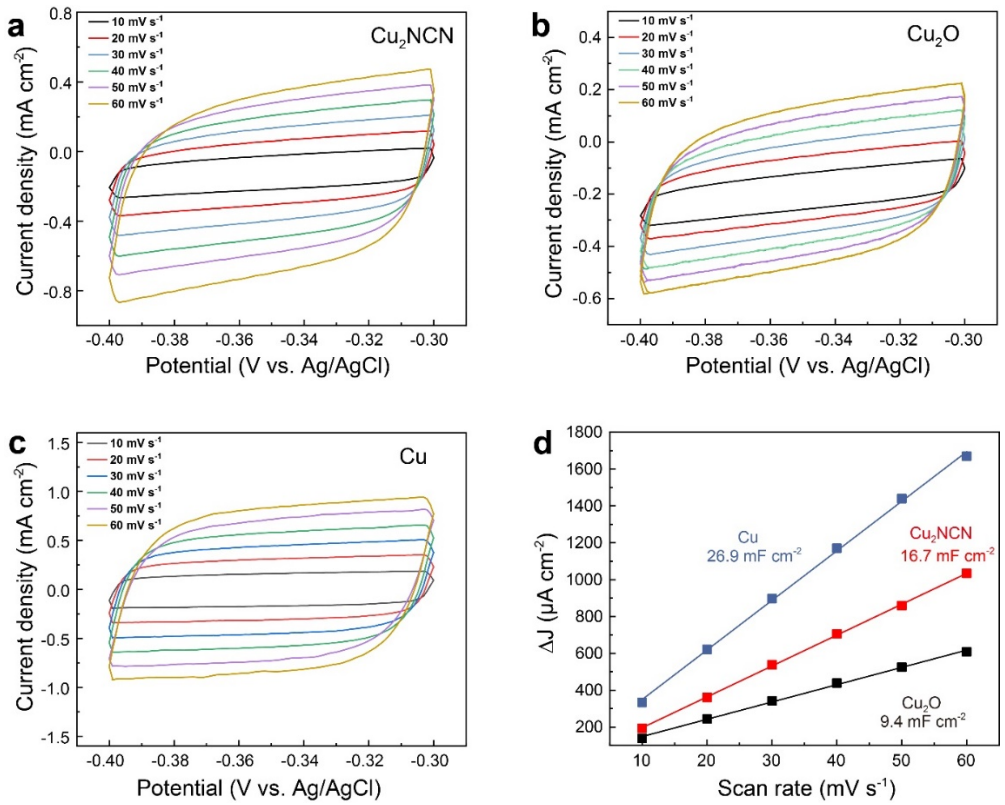

Supplementary Figure 24. Assessments on the specific electrochemically active surface areas. Cyclic voltammetry curve of (a) Cu_2NCN, (b) Cu_2O, and (c) Cu at different scan rates, and (d) the fitted slopes of these three samples.

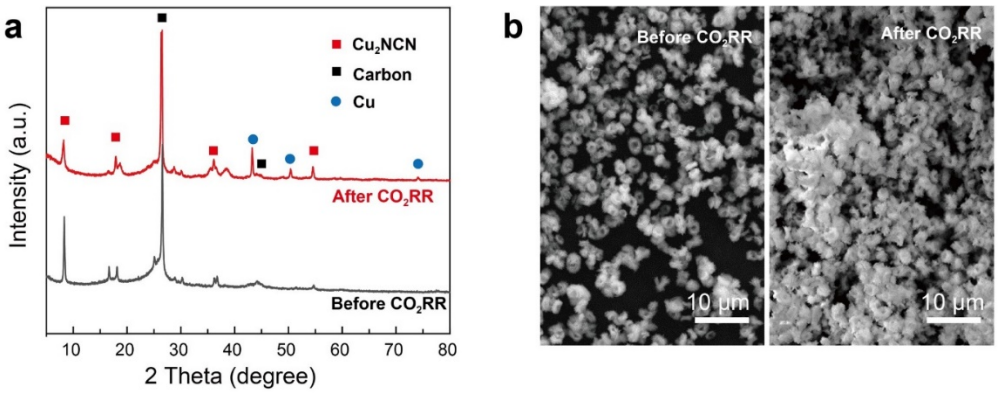

Supplementary Figure 25. Structure and morphology of Cu_2NCN after the CO_2RR electrolysis. (a) XRD pattern and (b) SEM images of Cu_2NCN before and after 10-hour electrolysis in a 5-cm^2 MEA-based electrolyzer with a total current of 400 mA.

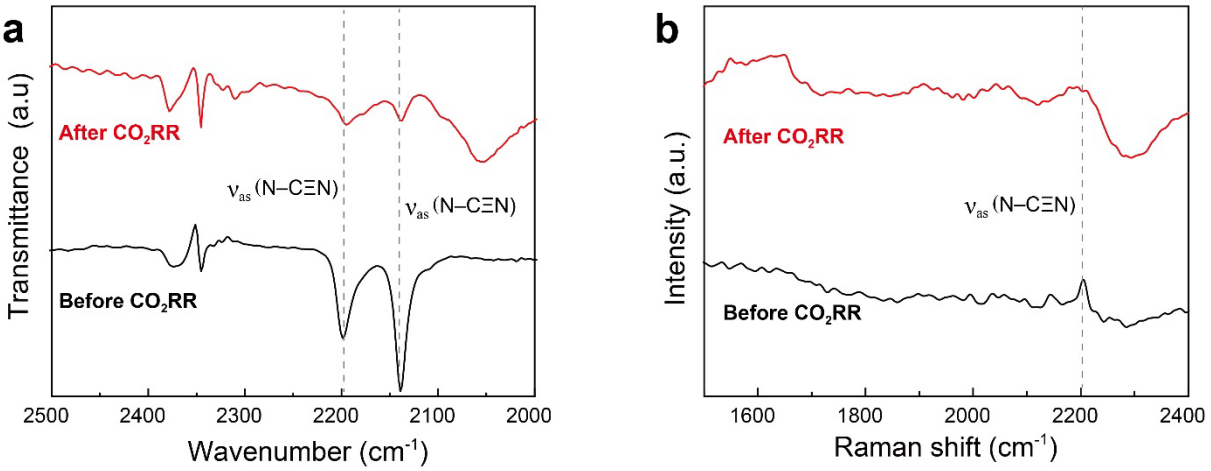

Supplementary Figure 26. Spectroscopic characterization on the stability of Cu_2NCN. (a) IR and (b) Raman spectra of Cu_2NCN before and after 10-hour electrolysis in a 5-cm^2 MEA-based electrolyzer with a total current of 400 mA.

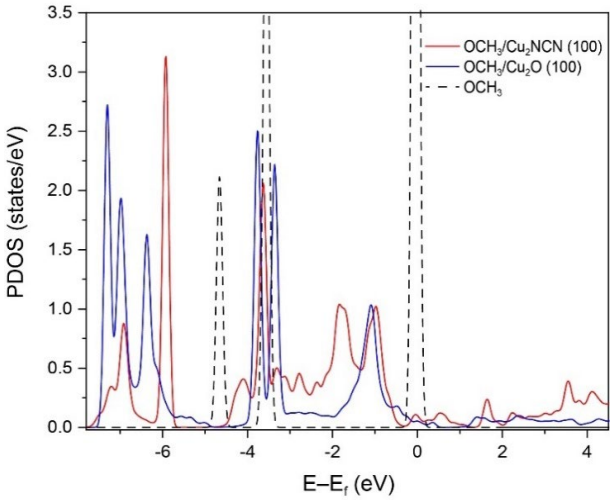

Supplementary Figure 27. PDOS of O *2p*-orbitals for free OCH_3 (dotted curve), adsorbed *OCH_3 on Cu_2O(100) (blue curve) and Cu_2NCN(100) (red curve).

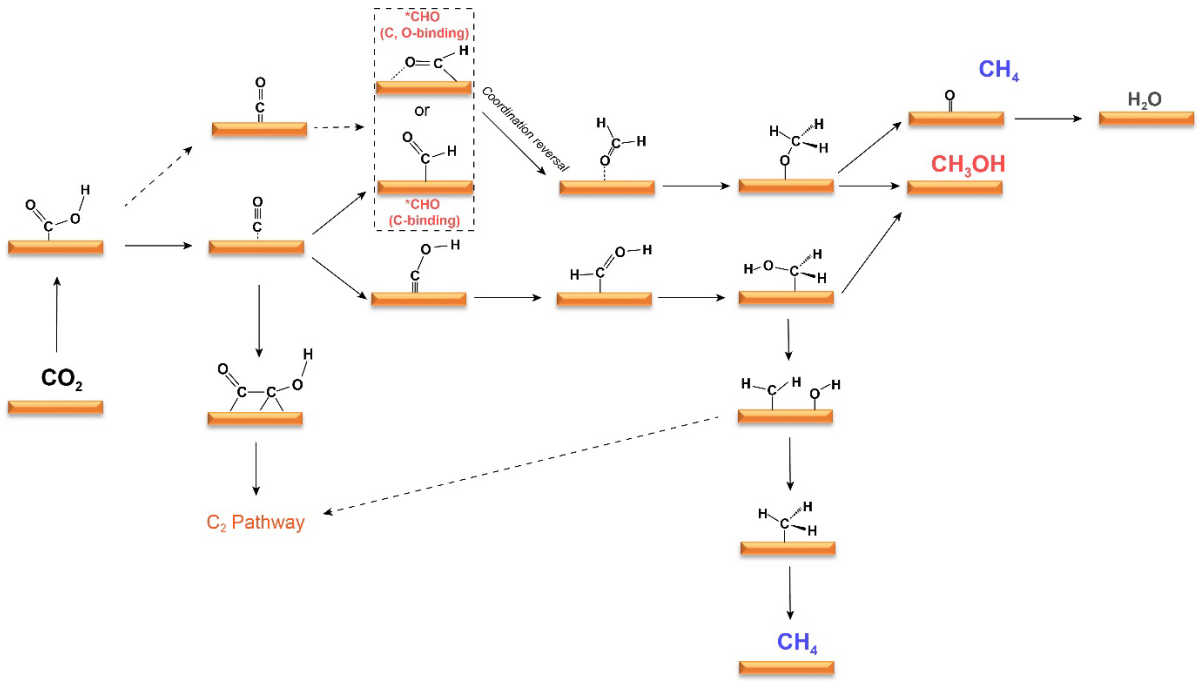

Supplementary Figure 28. Schematic illustration of possible CO_2RR pathways on Cu surface toward CH_4 and CH_3OH. The *COH-pathway is confirmed unfavorable on Cu_2NCN.

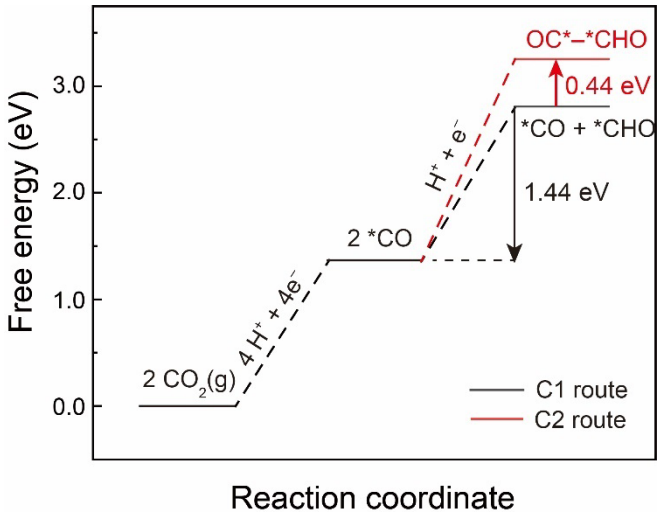

Supplementary Figure 29. Free energy profile of CO_2RR on Cu_2O (100). The C_1 and C_2 routes were indicated by black and red colors.

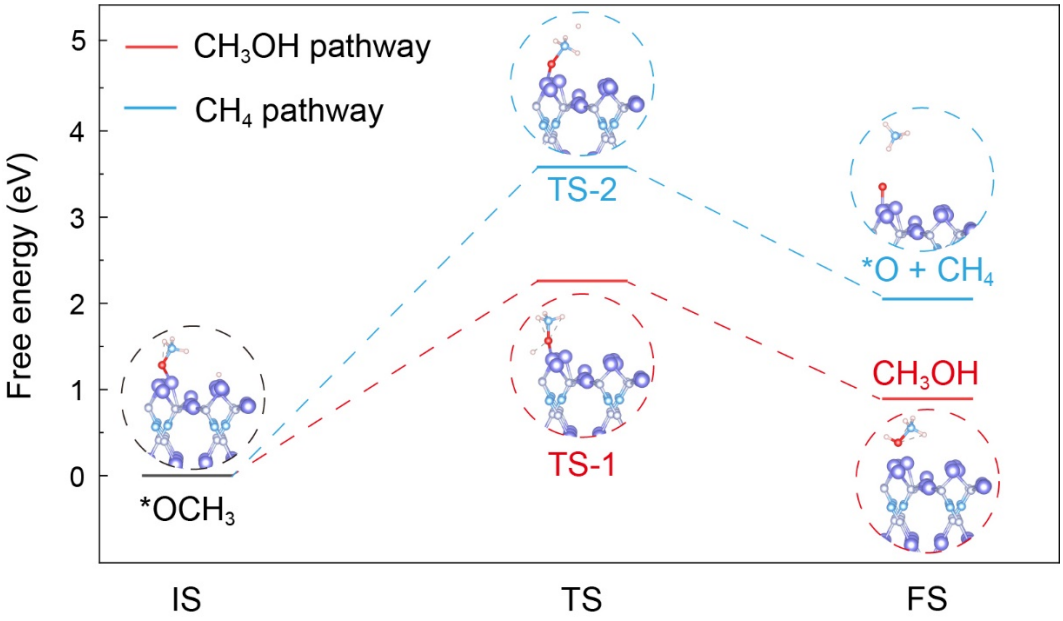

Supplementary Figure 30. Transition state studies on the hydrogenation of *OCH_3 on Cu_2NCN (100). Free energy corrections were performed at 298.15 K while the CHE model was not employed here.

Supplementary Tables

Supplementary Table 1. Crystallographic data and structure refinement for Cu_2NCN.

Stoichiometric formula	Cu_2NCN
Crystal system	monoclinic
Space group	*P*2/*m*
a, *b*, *c*, Å	11.064(9), 6.305(2), 4.109(2)
β, °	100.31(5)
Z	4
Radiation, Å	0.0197
Temperature, K	293
Number of frames	102
Range of data collection, °	−55.5 to 50
Tilt step, °	1
Precession angle, °	1
h, *k*, *l*	$-13 \leq h \leq 12$, $-7 \leq k \leq 7$, $-5 \leq l \leq 5$
g_{max}, S_g^{max}(matrix), S_g^{max}(refine), R_{Sg}	1.25, 0.01, 0.1, 0.4
Measured reflections	1459
Observed reflections ($I \geq 3\sigma(I)$)	747
Thickness (nm, refined)	492(4)
R_{obs}, wR_{obs}	0.0777, 0.0893
R_{all}, wR_{all}	0.1488, 0.0928
Maximum / minimum residual electrostatic potential, e/Å	0.43, −0.4

Supplementary Table 2. **Atomic coordinates and equivalent isotropic displacement parameters in Cu_2NCN.**

Atom	Wyck.	*x/a*	*y/b*	*z/c*	U_{eq}[Å^2]	Occu.
Cu1	4o	0.1332(3)	0.2490(5)	0.0678(6)	0.0138(8)	1
Cu2	1f	0	1/2	1/2	0.0151(15)	1
Cu3	1e	1/2	1/2	1	0.0195(16)	1
Cu4	1g	-1/2	0	1/2	0.0249(16)	1
Cu5	1c	0	0	1/2	0.0085(14)	1
N1	2n	0.1497(19)	1/2	0.333(3)	0.020(3)	1
N2	2n	0.3457(17)	1/2	0.747(3)	0.022(3)	1
N3	2m	-0.1466(8)	0	0.1860(2)	0.028(3)	1
N4	2m	-0.3433(8)	0	0.385(3)	0.033(3)	1
C1	2n	0.2567(18)	1/2	0.549(4)	0.025(2)	1
C2	2m	-0.2501(17)	0	0.280(3)	0.025(2)	1

Supplementary Table 3. **The N−C bond lengths in Cu_2NCN.**

Bond	Bond lengths / Å
C1−N1	1.35(3)
C1−N2	1.16(3)
C2−N3	1.23(3)
C2−N4	1.17(3)

Supplementary Table 4. EXAFS analyses. Fitting results (i.e., as-acquired values of structural parameters) for the first coordination shell (1 – 3 Å) of Cu Atoms in Cu_2NCN, Cu_2O, CuO, and Cu foil samples from Cu *K*-edge EXAFS Data. (***ΔE₀***: energy shift; *N*: coordination number; ⟨*R*⟩: interatomic distance; σ^2: Debye-Waller factor).

	Cu_2NCN	**Cu_2O**	**CuO**	**Cu foil**
ΔE₀ (eV)	9.2(9)	4.7(0)	8.3(8)	1.0(3)
$N_{Cu–N}$	1.8(6)			
$N_{Cu–C}$	0.0(1)			
$N_{Cu–O}$		1.3(7)	2.0(8)	
$N_{Cu–Cu}$	0.0	8.2(6)	3.6(3)	10.1(8)
$\langle R\rangle_{Cu–N}$ (Å)	1.892(7)			
$\langle R\rangle_{Cu–C}$ (Å)	2.589(9)			
$\langle R\rangle_{Cu–O}$ (Å)		1.858(1)	1.960(1)	
$\langle R\rangle_{Cu–Cu}$ (Å)		2.994(3)	2.983(5)	2.529(0)
$\sigma^2_{Cu–N}$ (Å^2)	0.0046(9)			
$\sigma^2_{Cu–C}$ (Å^2)	0.0106(6)			
$\sigma^2_{Cu–O}$ (Å^2)		0.0019(0)	0.0042(4)	
$\sigma^2_{Cu–Cu}$ (Å^2)		0.0195(5)	0.0168(5)	0.0083(6)
R-factor	0.0100(4)	0.0234(8)	0.0338(7)	0.0139(9)

Supplementary Table 5. Effective mass (*m) calculation and corresponding experimental value.** 1 Hartree = m_e = 9.1095×10^{-31} Kg. Lower effective mass of electron at CBM reveals a weaker interaction between the electrons and crystal field according to condensed matter physics, suggesting more pronounced electron delocalization[29].

System	Calculated *m** at CBM (Hartree)	Experimental value of *m** (Hartree)
Cu	0.85	0.90[30]
Cu_2O	0.81	0.66[31]
Cu_2NCN	0.25	n. d.

n.d.: Not determined.

Supplementary Table 6. Bond dissociation enthalpies (ΔH) of Cu–*O–CH_3. ΔH_{Cu-O} and ΔH_{O-C} were calculated on Cu_2O (100) and Cu_2NCN (100), calculation details were described in the methods.

Surface	ΔH_{Cu-O} (kJ·mol^{-1})	ΔH_{O-C} (kJ·mol^{-1})
Cu_2O (100)	497.2	313.4
Cu_2NCN (100)	245.0	305.1

Supplementary Table 7. Carbon-based product distributions for CO_2RR in MEA-based electrolyzers at a full-cell voltage of 3.4 V. Electrolysis was performed in 0.5 M $KHCO_3$, with a CO_2 flow speed of 30 mL·min^{-1}.

Product	Selectivity (%)
CH_3OH	70.0
CH_4	0.3
CO	13.1
HCOOH	4.2
C_2H_4	7.7
C_2H_5OH	4.1
CH_3COOH	0.6

Supplementary Table 8. Detailed crystal plane information of Cu_2NCN from XRD.

(h k l)	2-Theta (°)	D (Å)	Intensity (a.u.)	Note
(1 0 0)	8.116	10.8855	100	Strongest
(0 1 0)	14.034	6.3051	0	
(2 0 0)	16.272	5.4427	15.2	
(0 0 1)	21.971	4.0422	1.2	
(-1 0 1)	22.026	4.0323	0.8	
(3 0 0)	24.513	3.6285	10.7	
(1 0 1)	24.81	3.5857	0.3	
(-2 0 1)	24.957	3.565	0.1	
(0 1 1)	26.165	3.403	4.8	
(-1 1 1)	26.212	3.397	4.5	
(0 2 0)	28.285	3.1526	3.7	
(1 1 1)	28.615	3.1169	13.3	
(-2 1 1)	28.744	3.1033	12.9	
(1 2 0)	29.473	3.0281	8.6	
(2 0 1)	29.772	2.9984	10	
(-3 0 1)	29.979	2.9782	9.5	
(2 2 0)	32.803	2.728	9.8	
(4 0 0)	32.884	2.7214	0.2	
(2 1 1)	33.054	2.7078	1.7	
(-3 1 1)	33.242	2.6929	1.6	
(4 1 0)	35.912	2.4986	0	
(3 0 1)	36.072	2.4879	14.8	
(0 2 1)	36.101	2.4859	28.8	3rd strongest

(-1 2 1)	36.136	2.4836	29.6	2nd strongest
(-4 0 1)	36.316	2.4717	14.3	
(3 2 0)	37.771	2.3798	6.4	
(1 2 1)	37.973	2.3676	3.5	
(-2 2 1)	38.073	2.3616	3.2	
(3 1 1)	38.883	2.3142	1	
(-4 1 1)	39.112	2.3012	1.3	
(5 0 0)	41.441	2.1771	1.2	
(2 2 1)	41.53	2.1726	0	
(4 0 1)	43.237	2.0907	5.3	
(-5 0 1)	43.507	2.0784	5.4	
(4 2 0)	43.915	2.06	20.9	
(-1 0 2)	44.045	2.0543	3.3	
(0 0 2)	44.806	2.0211	6.3	
(-2 0 2)	44.922	2.0161	6.7	
(4 1 1)	45.68	1.9845	1.9	
(-5 1 1)	45.938	1.9739	1.6	
(3 2 1)	46.459	1.953	0.6	
(-4 2 1)	46.657	1.9451	0.7	
(1 0 2)	47.143	1.9262	0	
(-2 1 2)	47.296	1.9204	0	
(-3 0 2)	47.367	1.9176	0	
(0 3 1)	48.797	1.8647	0.9	
(-1 3 1)	48.825	1.8637	0.6	
(1 1 2)	49.434	1.8422	0	

(-3 1 2)	49.65	1.8347	0.1
(3 3 0)	50.117	1.8187	0
(6 0 0)	50.247	1.8142	3.8
(1 3 1)	50.278	1.8132	1.8
(-2 3 1)	50.359	1.8105	1.9
(2 0 2)	50.889	1.7929	0.4
(5 2 0)	50.932	1.7914	1.1
(5 0 1)	51.043	1.7878	1
(-4 0 2)	51.207	1.7825	0.3
(-6 0 1)	51.334	1.7784	1
(4 2 1)	52.474	1.7424	0.6
(-5 2 1)	52.707	1.7352	0.4
(2 1 2)	53.06	1.7245	0
(-1 2 2)	53.173	1.7211	3.1
(2 3 1)	53.176	1.721	0.4
(5 1 1)	53.21	1.72	0.6
(-3 3 1)	53.305	1.7172	0.4
(-4 1 2)	53.369	1.7153	0
(-6 1 1)	53.492	1.7116	0.5
(0 2 2)	53.836	1.7015	0
(-2 2 2)	53.938	1.6985	0.1
(4 3 0)	55.172	1.6634	0
(3 0 2)	55.845	1.6449	1
(-3 2 2)	56.089	1.6383	0
(-5 0 2)	56.242	1.6343	0.9

(3 3 1)	57.342	1.6055	0.3
(-4 3 1)	57.513	1.6011	0.3
(3 1 2)	57.887	1.5917	0
(-5 1 2)	58.275	1.582	0
(0 4 0)	58.507	1.5763	6.5
(6 2 0)	58.663	1.5725	1.7
(1 4 0)	59.177	1.56	1.2
(2 2 2)	59.241	1.5585	8.8
(5 2 1)	59.38	1.5551	0.3
(7 0 0)	59.384	1.5551	0.9
(6 0 1)	59.408	1.5545	0
(-4 2 2)	59.528	1.5516	8.5
(-6 2 1)	59.643	1.5489	0.4
(-7 0 1)	59.718	1.5471	0
(2 4 0)	61.161	1.5141	0.9
(6 1 1)	61.375	1.5093	0.7
(-7 1 1)	61.68	1.5026	0.6
(4 0 2)	61.834	1.4992	0.1
(-6 0 2)	62.3	1.4891	0.2
(4 3 1)	62.621	1.4822	0.5
(-5 3 1)	62.83	1.4778	0.5
(0 4 1)	63.271	1.4686	0.2
(-1 4 1)	63.294	1.4681	0.1
(4 1 2)	63.757	1.4585	0.1
(3 2 2)	63.766	1.4583	2.1

(-5 2 2)	64.133	1.4509	2.1
(-6 1 2)	64.215	1.4492	0
(3 4 0)	64.388	1.4457	0.9
(1 3 2)	65.699	1.42	0
(-3 3 2)	65.88	1.4166	0
(2 4 1)	67.02	1.3952	1.4
(7 2 0)	67.053	1.3946	1
(6 2 1)	67.075	1.3942	1.5
(-3 4 1)	67.132	1.3932	1.3
(-7 2 1)	67.366	1.3889	1.6
(7 0 1)	68.341	1.3714	0.2
(-1 0 3)	68.572	1.3674	0.1
(-2 0 3)	68.638	1.3662	0.1
(-8 0 1)	68.673	1.3656	0.2
(5 0 2)	68.741	1.3644	0
(4 4 0)	68.767	1.364	0
(5 3 1)	68.895	1.3618	0.2
(8 0 0)	68.957	1.3607	2.6
(-4 3 2)	69.031	1.3594	0
(-6 3 1)	69.137	1.3576	0.2
(-7 0 2)	69.27	1.3553	0
(4 2 2)	69.352	1.3539	2.9
(-6 2 2)	69.791	1.3464	2.7
(-3 0 3)	69.931	1.3441	0
(7 1 1)	70.17	1.3401	0.2

(-1 1 3)	70.398	1.3363	0.2
(-2 1 3)	70.464	1.3352	0.1
(-8 1 1)	70.498	1.3347	0.4
(3 4 1)	70.69	1.3315	2.8
(-4 4 1)	70.843	1.329	2.7
(0 1 3)	71.547	1.3177	0.3
(-3 1 3)	71.742	1.3146	0.2
(1 0 3)	72.098	1.3089	0.6
(-4 0 3)	72.422	1.3039	0.6
(3 3 2)	72.975	1.2954	0
(1 1 3)	73.886	1.2816	0.1
(-4 1 3)	74.207	1.2769	0.2
(5 4 0)	74.214	1.2768	0.3
(4 4 1)	75.468	1.2586	1.4
(7 2 1)	75.542	1.2576	1.9
(2 0 3)	75.618	1.2565	0.9
(-5 4 1)	75.659	1.2559	1.5
(-1 2 3)	75.763	1.2545	1.8
(-2 2 3)	75.827	1.2536	1.8
(-8 2 1)	75.86	1.2531	1.7
(5 2 2)	75.925	1.2522	0
(-1 4 2)	76.043	1.2505	1
(-5 0 3)	76.064	1.2503	1
(6 3 1)	76.097	1.2498	0.3
(8 2 0)	76.133	1.2493	0

(-7 3 1)	76.373	1.246	0.3
(-7 2 2)	76.434	1.2451	0.1
(6 0 2)	76.52	1.2439	1.1
(0 4 2)	76.591	1.243	1.8
(-2 4 2)	76.675	1.2418	2
(0 2 3)	76.881	1.239	0.5
(-3 2 3)	77.071	1.2364	0.5
(-8 0 2)	77.111	1.2359	1
(2 1 3)	77.377	1.2323	0.4
(-5 1 3)	77.819	1.2264	0.3
(4 3 2)	78.265	1.2205	0
(6 1 2)	78.272	1.2204	0
(-3 4 2)	78.48	1.2177	0
(-6 3 2)	78.686	1.215	0
(-8 1 2)	78.86	1.2128	0
(9 0 0)	79.116	1.2095	0.1
(1 2 3)	79.164	1.2089	0
(0 5 1)	79.565	1.2038	0.1
(-1 5 1)	79.585	1.2035	0.1
(8 1 1)	79.668	1.2025	0.1

Supplementary Table 9. Adsorption features for CO_2 at the different sites on Cu_2NCN (100). Generally, (100) surface has three kinds of sites: top, bridge and hollow sites. And the adsorption energy (E_{ad}), the nearest Cu−C distance (D_{Cu-C}) and the angle degree of O−C−O in CO_2 (θ_{O-C-O}) were employed for comparison.

Adsorption Site	**Top**	**Bridge**	**Hollow**
Top view	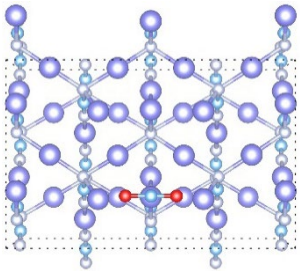	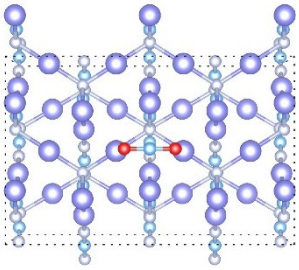	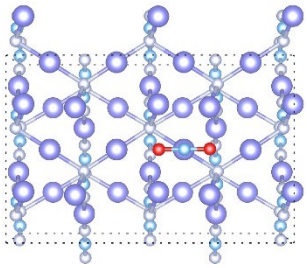
Side view	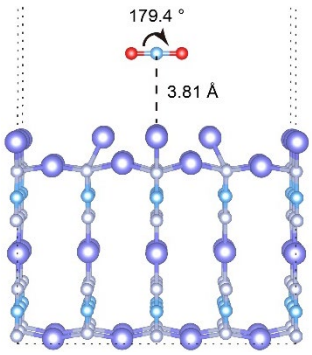	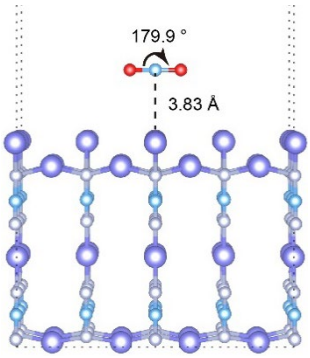	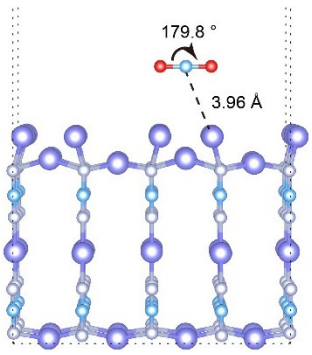
E_{ad} (eV)	−0.90	−0.06	−0.86
D_{Cu-C} (Å)	3.81	3.83	3.96
θ_{O-C-O} (°)	179.4	179.9	179.8

Supplementary Table 10. Assessments of three possible intermediates obtained after 2→3 process in Figure 5c.

Intermediates	ΔG (eV)
*CHO (C, O-binding)	0.02
*CHO (C-binding)	0.64
*COH	0.83

Supplementary Table 11. Assessments of three possible intermediates obtained after 3→4 process in Figure 5c.

Intermediates	ΔG (eV)
$*OCH_2$	1.10
*CHOH	1.13
$*C(=O)H_2$	1.61

Supplementary Table 12. Transition state (TS) studies on the hydrogenation of $*OCH_3$ on Cu_2NCN (100). Energy barrier was calculated by $G_{TS}-G_{IS}$, and relative free energy was calculated by $G_{FS}-G_{IS}$.

Pathway	Energy barrier (eV)	Relative free energy (eV)
$*OCH_3 + [H] \xrightarrow{TS-1} * + CH_3OH$	2.26	0.89
$*OCH_3 + [H] \xrightarrow{TS-2} *O + CH_4$	3.58	2.05

Supplementary Table 13. Frequency analysis for TS-1. Frequency calculations were performed in a stricter condition with the maximum force to be less than 0.01 eV·Å^{-1}.

No.	Frequency (cm^{-1})
1	3072.2
2	380.1
3	369.1
4	176.1
5	175.2
6	172.7
7	140.0
8	137.9
9	129.0
10	115.4
11	70.4
12	41.5
13	36.4
14	22.5
15	12.7
16	10.3
17	5.8
18 (imaginary frequency)	158.0i

Supplementary Table 14. Frequency analysis for TS-2. Frequency calculations were performed in a stricter condition with the maximum force to be less than 0.01 eV·Å^{-1}.

No.	Frequency (cm^{-1})
1	3206.3
2	3205.2
3	3039.2
4	1337.9
5	1334.1
6	1136.4
7	1040.7
8	1034.1
9	594.0
10	524.2
11	500.4
12	367.7
13	350.8
14	164.7
15	92.5
16	73.3
17	51.4
18 (imaginary frequency)	927.8i

Supplementary References

1. Newville, M. Fundamentals of XAFS. *Rev. Mineral. Geochem.* **78**, 33-74 (2014).
2. Hobson, A. There are no particles, there are only fields. *Amer. J. Phys.* **81**, 211-223 (2013).
3. McNaught, A. D. & Wilkinson, A. *Compendium of chemical terminology*, vol. 1669. Blackwell Science Oxford, 1997.
4. Parr, R. G. & Pearson, R. G. Absolute hardness: companion parameter to absolute electronegativity. *J. Am. Chem. Soc.* **105**, 7512-7516 (1983).
5. Pearson, R. G. Chemical hardness and density functional theory. *J. Chem. Sci.* **117**, 369-377 (2005).
6. Matito, E. & Putz, M. V. New link between conceptual density functional theory and electron delocalization. *J. Phys. Chem. A* **115**, 12459-12462 (2011).
7. Sablon, N., De Proft, F. & Geerlings, P. The linear response kernel of conceptual DFT as a measure of electron delocalisation. *Chem. Phys. Lett.* **498**, 192-197 (2010).
8. Rodriguez-Bautista, M., Vargas, R., Aquino, N. & Garza, J. Electron-density delocalization in many-electron atoms confined by penetrable walls: A Hartree–Fock study. *Int. J. Quantum. Chem.* **118**, e25571 (2018).
9. Kresse, G. & Furthmüller, J. Efficient iterative schemes for ab initio total-energy calculations using a plane-wave basis set. *Phys. Rev. B* **54**, 11169 (1996).
10. Kresse, G. & Joubert, D. From ultrasoft pseudopotentials to the projector augmented-wave method. *Phys. Rev. B* **59**, 1758 (1999).
11. Perdew, J. P., Burke, K. & Ernzerhof, M. Generalized gradient approximation made simple. *Phys. Rev. Lett.* **77**, 3865-3868 (1996).
12. Giannozzi, P. & Baroni, S. Vibrational and dielectric properties of C_{60} from density-functional perturbation theory. *J. Chem. Phys.* **100**, 8537-8539 (1994).
13. Wang, V., Xu, N., Liu, J.-C., Tang, G. & Geng, W.-T. VASPKIT: A user-friendly interface facilitating high-throughput computing and analysis using VASP code. *Comput. Phys. Commun.* **267**, 108033 (2021).
14. Ong, S. P., *et al.* Python Materials Genomics (pymatgen): A robust, open-source python library for materials analysis. *Comput. Mater. Sci.* **68**, 314-319 (2013).
15. Mathew, K., Sundararaman, R., Letchworth-Weaver, K., Arias, T. A. & Hennig, R. G. Implicit solvation model for density-functional study of nanocrystal surfaces and reaction pathways. *J. Chem. Phys.* **140**, 084106 (2014).
16. Mathew, K., Kolluru, V. S. C., Mula, S., Steinmann, S. N. & Hennig, R. G. Implicit self-consistent electrolyte model in plane-wave density-functional theory. *J. Chem. Phys.* **151**, 234101 (2019).
17. Gauthier, J. A., *et al.* Challenges in modeling electrochemical reaction energetics with polarizable continuum models. *ACS Catal.* **9**, 920-931 (2018).
18. Wang, S., *et al.* Cu_2O/CuS Nanocomposites Show Excellent Selectivity and Stability for Formate Generation via Electrochemical Reduction of Carbon Dioxide. *ACS Mater. Lett.* **3**, 100-109 (2020).
19. Henkelman, G., Uberuaga, B. P. & Jónsson, H. A climbing image nudged elastic band method for finding saddle points and minimum energy paths. *J. Chem. Phys.* **113**, 9901-9904 (2000).
20. Humphrey, W., Dalke, A. & Schulten, K. VMD: Visual molecular dynamics. *J. Mol. Graph.* **14**, 33-38 (1996).
21. Levine, B. G., Stone, J. E. & Kohlmeyer, A. Fast analysis of molecular dynamics trajectories with graphics processing units—Radial distribution function histogramming. *J. Comput. Phys.* **230**, 3556-3569 (2011).
22. Giannozzi, P. & Baroni, S. Vibrational and dielectric properties of C_{60} from density-functional

perturbation theory. *J. Chem. Phys.* **100**, 8537-8539 (1994).

23. Karhánek, D., Bučko, T. & Hafner, J. A density-functional study of the adsorption of methane-thiol on the (111) surfaces of the Ni-group metals: II. Vibrational spectroscopy. *J. Phys. Condens. Matter* **22**, 265006 (2010).
24. Görne, A. L., George, J., Van Leusen, J. & Dronskowski, R. Synthesis, Crystal structure, polymorphism, and magnetism of $Eu(CN_3H_4)_2$ and first evidence of $EuC(NH)_3$. *Inorganics* **5**, 10 (2017).
25. Janine George & Richard Dronskowski. JaGeo/IR: IR. (2019) doi:10.5281/zenodo.3241592.
26. Zheng, L., Xu, Y., Jin, D. & Xie, Y. Novel metastable hexagonal MoO_3 nanobelts: Synthesis, photochromic, and electrochromic properties. *Chem. Mater.* **21**, 5681-5690 (2009).
27. Lü, X.*, et al.* Improved-performance dye-sensitized solar cells using Nb-doped TiO_2 electrodes: Efficient electron injection and transfer. *Adv. Funct. Mater.* **20**, 509-515 (2010).
28. Qiao, X.*, et al.* Nonlinear optical effects in two mercury cyanamide/guanidinium chlorides $Hg_3(NCN)_2Cl_2$ and $Hg_2(C(NH_2)_3)Cl_5$. *J. Mater. Chem. C* **9**, 967-974 (2021).
29. Bardeen, J. & Shockley, W. Deformation potentials and mobilities in non-polar crystals. *Phys. Rev.* **80**, 72-80 (1950).
30. Knapp, J. A., Himpsel, F. J. & Eastman, D. E. Experimental energy band dispersions and lifetimes for valence and conduction bands of copper using angle-resolved photoemission. *Phys. Rev. B* **19**, 4952-4964 (1979).
31. Ching, W. Y., Xu, Y. N. & Wong, K. W. Ground-state and optical properties of Cu_2O and CuO crystals. *Phys. Rev., B Condens. Matter* **40**, 7684-7695 (1989).